THE JOURNAL OF
PHYSICAL CHEMISTRY C

pubs.acs.org/JPCC Article

Simulating Electron Dynamics in Open Quantum Systems under Magnetic Fields

Tal Maaravi and Oded Hod*

Cite This: *J. Phys. Chem. C* 2020, 124, 8652−8662 Read Online

ABSTRACT: A method for simulating electronic transport through molecular junctions subjected to time-dependent external magnetic fields is developed. The method constitutes a merge of the magnetic extended Hückel theory and the driven Liouville von Neumann approach. The former accounts for orbital magnetic effects in molecular systems whereas the latter enables simulating electron dynamics in open quantum systems within single-particle treatments. The method is demonstrated on simplistic model systems of Aharonov−Bohm molecular interferometers consisting of hydrogen rings connected to two hydrogen chain leads. Depending on the angular separation between the leads and the value of the magnetic flux, the current flowing through the system can be switched-on or -off by the application of the external field. During the transient dynamics period, whose extent depends on the nature and strength of the coupling between the ring and the leads, the system exhibits oscillatory currents before reaching the new steady-state. Visualizing the electron density variations in the transient period reveals that dynamic interference effects dictate the transport characteristics of the system. These results demonstrate the capabilities of the developed methodology to study fundamental transport mechanisms of complex molecular junctions subjected to time-dependent external magnetic fields. This, in turn, may lead to the rational design of molecular switches with controllable operational frequencies.

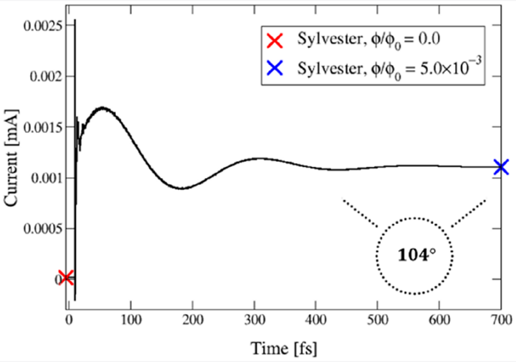

■ INTRODUCTION

The field of molecular electronics[1−6] provides important fundamental insights on the physics of low-dimensional systems embedded in complex environments and subjected to external perturbations. Furthermore, it holds great promise for the miniaturization of electronic devices, beyond the classical limits of silicon technology.[7] Typical realizations of molecular electronics devices include a single molecule (or a molecular monolayer) coupled to particle and heat reservoirs via metallic leads. The system can then be driven out of equilibrium by applying a voltage and/or thermal bias between the reservoirs. To control the electronic transport through the molecule, various schemes have been suggested, including: (i) modifying the chemical structure of the active molecule;[8−14] (ii) varying its coupling to the leads;[15−18] (iii) applying gate potentials;[19−22] and (iv) introducing electromagnetic fields.[23−25] These may lead to diverse functionalities, such as conductance switching,[26−29] current routing,[30] rectification,[31−34] heat pumping,[35−37] and single-molecule magnetoresistance.[38]

One of the intriguing aspects of molecular junctions is that their dimensions are typically comparable or smaller than the coherence length of the transporting electrons. This allows the utilization of interference effects for the design and control of unique behaviors.[23,39−49] A natural platform to realize such effects are molecular rings, where current can flow through multiple paths and interfere (constructively or destructively) before exiting the system. Such rings are prone to the effect of magnetic fields via the Aharonov−Bohm (AB) effect,[50−55] where the phase of clockwise and counterclockwise propagating electrons is oppositely affected. In this respect, much work has been done to study the conditions required to achieve magnetic control over molecular junctions. In particular, it was shown that, despite the unfeasibly large magnetic fields required to achieve a full AB interference cycle in molecular rings, in the weak molecule−lead coupling regime conductance can be switched with experimentally accessible field intensities.[40,55−59]

Notably, these studies focused on steady-state conditions, where the current flowing through the system is time-independent. Nevertheless, in recent years much attention has been given to dynamical effects in molecular junctions.[60−65] Such temporal effects are important as they dictate the transient dynamics of the proposed devices, their response time to external control parameters, and their behavior under time-

Received: February 27, 2020
Published: March 17, 2020

https://dx.doi.org/10.1021/acs.jpcc.0c01706
J. Phys. Chem. C 2020, 124, 8652−8662

varying perturbations such as alternating current and/or electromagnetic pulses that can lead to novel functionalities.

The purpose of the present paper is to present a methodology for the simulation of electron dynamics in molecular junctions subject to (generally time-dependent) magnetic fields. To this end, we merge the recently developed driven Liouville von Neumann (DLvN)[17,66−69] approach for simulating electron dynamics in open quantum systems with the magnetic extended Hückel theory (MEHT)[57,59] for studying the AB effect in molecular rings. This allows us to investigate dynamical aspects of coherence and interference effects and to demonstrate switching functionality in molecular junctions subject to external magnetic fields. We further investigate the leads−ring coupling effect on the response of the current flowing through the system to the switch-on of the magnetic field. When the distance between the ring and the leads is increased, a resonant tunneling junction is formed, where a nearly degenerate pair of sharp ring levels participate in the transport process.[17,70] This allows us to achieve dynamical current switching at feasible magnetic flux values.[56,59]

■ METHODOLOGY

System Partitioning. As mentioned above, our tool-of-choice for performing time-dependent simulations of electron dynamics in open quantum systems is the driven Liouville von Neumann approach.[17,66−69] Within this approach, nonequilibrium boundary conditions are imposed at the edges of noninteracting fully atomistic finite molecular junction models, effectively coupling them to implicit Fermionic reservoirs of different chemical potentials and electronic temperatures. To this end, the system is artificially partitioned into three sections (for a two-lead setup) including the left lead (L), the right lead (R), and an (extended-) molecule (EM). The latter includes the active molecule dressed by its adjacent lead parts, chosen to be sufficiently large to converge the electronic properties of the whole section with respect to their size to within a required accuracy. This buffers the molecule from the direct effect of the applied boundary conditions, as described below. The resulting single-particle Hamiltonian and overlap matrices, given in a localized basis-set representation, have the following general block form:

$$\boldsymbol{H} = \begin{pmatrix} \boldsymbol{H}_L & \boldsymbol{V}_{L,EM} & \boldsymbol{0} \\ \boldsymbol{V}_{EM,L} & \boldsymbol{H}_{EM} & \boldsymbol{V}_{EM,R} \\ \boldsymbol{0} & \boldsymbol{V}_{R,EM} & \boldsymbol{H}_R \end{pmatrix}; \quad \boldsymbol{S} = \begin{pmatrix} \boldsymbol{S}_L & \boldsymbol{S}_{L,EM} & \boldsymbol{0} \\ \boldsymbol{S}_{EM,L} & \boldsymbol{S}_{EM} & \boldsymbol{S}_{EM,R} \\ \boldsymbol{0} & \boldsymbol{S}_{R,EM} & \boldsymbol{S}_R \end{pmatrix} \tag{1}$$

where $\boldsymbol{H}_L$, $\boldsymbol{H}_{EM}$, $\boldsymbol{H}_R$ and $\boldsymbol{S}_L$, $\boldsymbol{S}_{EM}$, $\boldsymbol{S}_R$ are the left lead, extended molecule, and right lead Hamiltonian and overlap matrix representations, respectively. $\boldsymbol{V}_{n,m}$, $\boldsymbol{S}_{n,m}$ ($n \neq m$; $n,m = L, EM, R$) are the inter-section coupling and overlap matrices, where the direct coupling and overlap between the two leads are neglected.

Magnetic Extended Hückel Theory. For our Hamiltonian operator we use the MEHT[57,59] that incorporates magnetic terms within the extended Hückel (EH) Hamiltonian. In the latter a Slater-type orbitals (STO) basis-set is used for the construction of the overlap matrix and the Hamiltonian off diagonal elements are given by $H_{ij} = K\frac{H_{ii}+H_{jj}}{2}S_{ij}$, where $K = 1.75$ is a fitting parameter, S_{ij} is the overlap between atomic centers i and j and H_{ii} are the Hamiltonian diagonal elements approximated as the ionization potential of atomic center i. We note that the overlap matrix elements between basis functions residing on different atomic sites decays with increasing interatomic distance. Hence, the coupling between the ring and the leads can be controlled by varying the relative position of the leads and the ring. $\boldsymbol{H}^{EH}$ is then augmented by linear and quadratic magnetic terms as follows:

$$\boldsymbol{H} = \boldsymbol{H}^{EH} + i\mu_B B_x\left(y\frac{\partial}{\partial z} - z\frac{\partial}{\partial y}\right) + \frac{q^2 {B_x}^2}{8m_e}(y^2 + z^2) \tag{2}$$

Here, B_x is a uniform magnetic field applied (without loss of generality) along the x direction, $q = |e|$ and m_e are the electron charge and mass, respectively, $\mu_B = q\hbar/2m_e$ is the Bohr magneton, and $\hbar = h/2\pi$ is the reduced Plank constant (for a full derivation of this expression, see ref 59). We note that within this model, only orbital magnetic interactions are taken into account and Zeeman spin splitting, as well as spin−orbit coupling effects, are neglected. Each of the STOs is multiplied by an appropriate gauge factor of the form $G_\alpha = \mathrm{e}^{-(iq/2\hbar)B_x(z_\alpha y - y_\alpha z)}$, with y_α and z_α being the y and z coordinates of nucleus α, around which the STO basis-function is centered.[59] This forms a gauge invariant (GI) STO basis-set[32,33] such that the effect of the finite size of the basis-set on the calculated magnetic phase is compensated. To simplify the Hamiltonian and overlap matrix elements calculation, we adopt the London approximation,[71,72] where for each pair of STO centers $\boldsymbol{R}_\alpha$ and $\boldsymbol{R}_\beta$, the gauge factors are taken outside the real-space integration and are evaluated at their midpoint, $\frac{1}{2}(\boldsymbol{R}_\alpha + \boldsymbol{R}_\beta)$ (for details see ref 59). The resulting matrix elements are given by:

$$\bar{H}_{1\alpha,2\beta} \approx \frac{1}{2}[H_{1\alpha,2\beta}\tilde{G}_{\alpha\beta} + H_{1\beta,2\alpha}\tilde{G}_{\beta\alpha}]; \quad \bar{S}_{1\alpha,2\beta} \approx S_{1\alpha,2\beta}\tilde{G}_{\alpha\beta} \tag{3}$$

where $H_{1\alpha,2\beta}$ and $S_{1\alpha,2\beta}$ are the gauge variant EH Hamiltonian and overlap matrix elements, respectively, of basis functions 1 and 2 centered around atomic positions α and β, and $\tilde{G}_{\alpha\beta} = \mathrm{e}^{(iq/2\hbar)B_x(z_\alpha y_\beta - y_\alpha z_\beta)}$.

Driven Liouville von Neumann Approach. Since the MEHT utilizes a nonorthogonal basis-set, a primary block-diagonalization procedure is required to ensure that the DLvN boundary conditions are applied at the far edges of the systems and do not directly interfere with the dynamics of the extended molecule region.[68,73] To this end, the localized STO basis-functions of the EM section are recast in a form that is mutually orthogonal to those of the lead sections. The transformation matrix to the block diagonal basis has the following form:

$$\boldsymbol{U}_b = \begin{pmatrix} \boldsymbol{I}_L & -\boldsymbol{S}_L^{-1}\boldsymbol{S}_{L,EM} & \boldsymbol{0} \\ \boldsymbol{0} & \boldsymbol{I}_{EM} & \boldsymbol{0} \\ \boldsymbol{0} & -\boldsymbol{S}_R^{-1}\boldsymbol{S}_{R,EM} & \boldsymbol{I}_R \end{pmatrix} \tag{4}$$

where $\boldsymbol{I}_L$, $\boldsymbol{I}_R$, and $\boldsymbol{I}_{EM}$ are the unit matrices of the dimensions of the left and right leads and the EM, respectively. The corresponding Hamiltonian and overlap matrices in the block diagonal basis are then given by $\tilde{\boldsymbol{H}} = \boldsymbol{U}_b^\dagger \boldsymbol{H}\boldsymbol{U}_b$ and $\tilde{\boldsymbol{S}} = \boldsymbol{U}_b^\dagger \boldsymbol{S}\boldsymbol{U}_b$.[74]

In order to apply appropriate boundary conditions, a site-to-state transformation is further invoked, moving to a representation, where the leads eigenstates are coupled to the eigenstates of the EM section. The corresponding unitary transformation matrix has the following block form:[66,68]

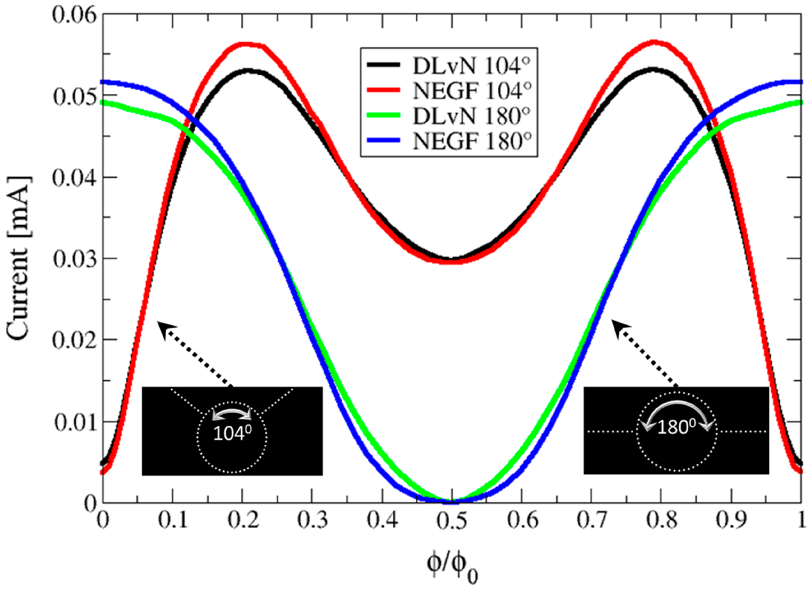

Figure 1. Steady-state current (obtained under a bias voltage of 1 V) vs the normalized magnetic flux threading an extended Hückel 52 hydrogen ring of diameter of 1.66 nm that is strongly coupled to 300 hydrogen atom chain leads arranged at angular separations of 180° and 104° calculated within the DLvN (green and black curves, respectively) and NEGF (blue and red curves, respectively) approaches. The geometries of the EM sections of the two configurations at the vicinity of the ring are presented in the insets.

$$\boldsymbol{U} = \begin{pmatrix} \boldsymbol{U}_L & \boldsymbol{0} & \boldsymbol{0} \\ \boldsymbol{0} & \boldsymbol{U}_{EM} & \boldsymbol{0} \\ \boldsymbol{0} & \boldsymbol{0} & \boldsymbol{U}_R \end{pmatrix} \tag{5}$$

where $\boldsymbol{U}_n$ (n = L, EM, R) are the unitary diagonalizing transformation matrices of the individual sections with appropriate dimensions, such that $\tilde{\tilde{\boldsymbol{H}}}_n = \boldsymbol{U}_n^\dagger \tilde{\boldsymbol{H}}_n \boldsymbol{U}_n$ are diagonal matrices, holding the n^{th} section eigenvalues on their main diagonal, and $\tilde{\tilde{\boldsymbol{S}}}_n = \boldsymbol{U}_n^\dagger \tilde{\boldsymbol{S}}_n \boldsymbol{U}_n = \boldsymbol{I}_n$.

In this so-called "state representation", the DLvN equation of motion has the following form:[66,68]

$$\frac{\mathrm{d}\tilde{\tilde{\boldsymbol{\rho}}}}{\mathrm{d}t} = -\frac{i}{\hbar}\left[\begin{pmatrix} \tilde{\tilde{\boldsymbol{H}}}_L & \tilde{\tilde{\boldsymbol{V}}}_{L,EM} & \boldsymbol{0} \\ \tilde{\tilde{\boldsymbol{V}}}_{EM,L} & \tilde{\tilde{\boldsymbol{H}}}_{EM} & \tilde{\tilde{\boldsymbol{V}}}_{EM,R} \\ \boldsymbol{0} & \tilde{\tilde{\boldsymbol{V}}}_{R,EM} & \tilde{\tilde{\boldsymbol{H}}}_R \end{pmatrix}, \begin{pmatrix} \tilde{\tilde{\boldsymbol{\rho}}}_L & \tilde{\tilde{\boldsymbol{\rho}}}_{L,EM} & \tilde{\tilde{\boldsymbol{\rho}}}_{L,R} \\ \tilde{\tilde{\boldsymbol{\rho}}}_{EM,L} & \tilde{\tilde{\boldsymbol{\rho}}}_{EM} & \tilde{\tilde{\boldsymbol{\rho}}}_{EM,R} \\ \tilde{\tilde{\boldsymbol{\rho}}}_{R.L} & \tilde{\tilde{\boldsymbol{\rho}}}_{R,EM} & \tilde{\tilde{\boldsymbol{\rho}}}_R \end{pmatrix}\right]$$
$$- \Gamma \begin{pmatrix} \tilde{\tilde{\boldsymbol{\rho}}}_L - \tilde{\tilde{\boldsymbol{\rho}}}_L^0 & \frac{1}{2}\tilde{\tilde{\boldsymbol{\rho}}}_{L,EM} & \tilde{\tilde{\boldsymbol{\rho}}}_{L,R} \\ \frac{1}{2}\tilde{\tilde{\boldsymbol{\rho}}}_{EM,L} & \boldsymbol{0} & \frac{1}{2}\tilde{\tilde{\boldsymbol{\rho}}}_{EM,R} \\ \tilde{\tilde{\boldsymbol{\rho}}}_{R,L} & \frac{1}{2}\tilde{\tilde{\boldsymbol{\rho}}}_{R,EM} & \tilde{\tilde{\boldsymbol{\rho}}}_R - \tilde{\tilde{\boldsymbol{\rho}}}_R^0 \end{pmatrix} \tag{6}$$

where $\tilde{\tilde{\boldsymbol{\rho}}}$ is the state-representation of the single-particle density matrix. The first term on the right-hand side of eq 6 represents the unitary dynamics of the closed system, whereas the second term imposes the boundary conditions on the lead sections. This is done by constantly driving their occupations toward the equilibrium Fermi–Dirac distribution (appearing on the main diagonal of the diagonal target density matrix blocks, $\tilde{\tilde{\boldsymbol{\rho}}}_{L/R}^0$) of the particle reservoir to which they are implicitly coupled.[68] Correspondingly, their coherences are dampened at the same rate, Γ, which can be extracted from the electronic properties of the implicit reservoirs.[69]

Driving Rate. For simplicity, in the present study we set the value of $\hbar\Gamma$ to be in the order of the largest lead interlevel spacing within the Fermi transport window (explicit values are provided in the Results and Discussion section below).[75−81] The validity of this choice is tested by verifying that the density of states of the semi-infinite lead is well represented (within the transport window) by the density of states of the corresponding finite lead model calculated with Lorentzian level broadening of width $\hbar\Gamma$ (see Supporting Information, section 1). We further verify that our transport results are sufficiently insensitive to the specific choice of the driving rate in this regime (see Supporting Information, section 1).

Initial Conditions. In the simulations presented below, we start at steady-state in the absence of a magnetic field and follow the transient response of the studied systems upon an abrupt switch-on of the field. The initial steady-state density matrix can be obtained by setting $\frac{\mathrm{d}\tilde{\tilde{\boldsymbol{\rho}}}}{\mathrm{d}t} = 0$ in eq 6, resulting in the following Sylvester equation (see Appendix A for a detailed derivation):[75,79,81]

$$\left[-\frac{i}{\hbar}\tilde{\tilde{\boldsymbol{H}}} - \frac{\Gamma}{2}(\boldsymbol{L} + \boldsymbol{R})\right]\tilde{\tilde{\boldsymbol{\rho}}}^{sts} + \tilde{\tilde{\boldsymbol{\rho}}}^{sts}\left[\frac{i}{\hbar}\tilde{\tilde{\boldsymbol{H}}} - \frac{\Gamma}{2}(\boldsymbol{L} + \boldsymbol{R})\right] = -\Gamma\tilde{\tilde{\boldsymbol{\rho}}}^0 \tag{7}$$

Here,

$$\boldsymbol{L} = \begin{pmatrix} \boldsymbol{I}_L & \boldsymbol{0} & \boldsymbol{0} \\ \boldsymbol{0} & \boldsymbol{0} & \boldsymbol{0} \\ \boldsymbol{0} & \boldsymbol{0} & \boldsymbol{0} \end{pmatrix}; \quad \boldsymbol{R} = \begin{pmatrix} \boldsymbol{0} & \boldsymbol{0} & \boldsymbol{0} \\ \boldsymbol{0} & \boldsymbol{0} & \boldsymbol{0} \\ \boldsymbol{0} & \boldsymbol{0} & \boldsymbol{I}_R \end{pmatrix} \tag{8}$$

are the projection matrices onto the left and right lead states, respectively, the target density matrix is given by

$$\tilde{\tilde{\boldsymbol{\rho}}}^{0} = \begin{pmatrix} \tilde{\tilde{\boldsymbol{\rho}}}_{L}^{0} & \mathbf{0} & \mathbf{0} \\ \mathbf{0} & \mathbf{0} & \mathbf{0} \\ \mathbf{0} & \mathbf{0} & \tilde{\tilde{\boldsymbol{\rho}}}_{R}^{0} \end{pmatrix} \tag{9}$$

and $\tilde{\tilde{\boldsymbol{\rho}}}^{sts}$ is the desired steady-state density matrix given in the state-representation.

Current Calculation. Both the steady-state current and the time-dependent current are calculated via the following expression (for a detailed derivation see Appendix B):

$$J(t) = \frac{|e|}{\hbar} \sum_{i}^{N_{EM}} \left\{ \sum_{j}^{N_L} \mathrm{Im}\{[\tilde{\tilde{\mathbf{V}}}_{L,EM}]_{j,i}^{*} [\tilde{\tilde{\boldsymbol{\rho}}}_{L,EM}]_{j,i}(t)\} + \sum_{j}^{N_R} \mathrm{Im}\{[\tilde{\tilde{\mathbf{V}}}_{EM,R}]_{i,j}^{*} [\tilde{\tilde{\boldsymbol{\rho}}}_{EM,R}]_{i,j}(t)\} \right\} \tag{10}$$

Here, the first term on the right-hand side represent the current flowing into the extended molecule section from the left lead and the second term represent the corresponding current exiting the extended molecule section into the right lead. Their average is defined as the total current flowing through the extended molecule section. To evaluate the steady state current, the density matrix obtained from the solution of eq 7, $\tilde{\tilde{\boldsymbol{\rho}}}^{sts}$, is inserted in eq 10, whereas for the time-dependent currents the instantaneous density matrix obtained from propagating eq 6 is used.

■ RESULTS AND DISCUSSION

To demonstrate the performance of the developed methodology we consider a simplistic model of a molecular ring of diameter 1.66 nm consisting of 52 hydrogen atoms (see the insets of Figure 1). The ring, along with two 300 atoms long linear hydrogen chains, constitutes the extended molecule section. The interatomic separation within the ring and within the chains are taken to be 1 Å. The extended molecule is coupled at the far edge of the two atomic chains to 2500 atoms hydrogen chain lead sections (see Supporting Information, section 2 for convergence tests with respect to this parameter), where the last atom in the EM chain is 1 Å distant from the first atom in the corresponding lead. In all calculations the electronic temperature was set to 300 K, a 1 V bias voltage was applied, and a driving rate of $\Gamma = 0.05$ fs^{-1} was used (see Supporting Information, section 1). The EH parameters that were used in the construction of the Hamiltonian and overlap matrices of the Hydrogen systems are IP = −13.6 eV for the ionization potential and $\zeta = 1.3$ au for the STO exponent.[82] The propagation of eq 6 has been performed using a fifth order Runge−Kutta adaptive time-step scheme,[83] where the initial time-step was set to 0.01 fs. For computational efficiency, a bandwidth cutoff has been employed in all calculations, where only a subset of the system's energy levels is considered. Within this procedure, energy levels that reside well beyond the Fermi-transport window are being excluded, with cutoff size of $|V_b + 2W|$ around the Fermi energy of the entire finite model system. We use a value of $W = 5$ eV, which provides reasonably converged currents (convergence tests are provided in Supporting Information section 3).

We first consider two configurations in the strong coupling regime, where all interatomic distances are uniformly taken to be 1 Å, with two lead angular separations of 180° and 104° as shown in Figure 1. The full AB transport periods of the two systems are presented in Figure 1, where the steady-state currents are plotted against the normalized magnetic flux threading the rings' cross sections. For the circle radius considered herein, a full AB cycle is obtained at a magnetic field of

$$B = \frac{\phi_0}{S} = 1922\ T$$

where

$$\phi_0 = \frac{h}{q} \approx 4.1357 \times 10^{-15}\ \mathrm{Wb}$$

is the magnetic flux quantum of the electrons. For the 180° connected system (green curve), the zero magnetic field current is high, due to constructive interference.[56] Upon the application of a magnetic field, the current reduces such that at half the AB period it is completely suppressed. Further increase of the magnetic field intensity results in current increase until full recovery is obtained at the full AB period. As for the 104° system (black curve), the steady-state current behavior with increasing magnetic fields is also periodic with ϕ_0 and symmetric around $\phi/\phi_0 = 0.5$. However, the steady state current in the absence of an external magnetic field is lower than the corresponding steady-state current of its 180° counterpart due to destructive interference that occurs in this configuration.[23,39,40] Applying a magnetic field results in an initial increase of the current until a maximum is reached at $\phi/\phi_0 \approx 0.25$. Further increase of the magnetic flux leads to a local minimum in the current obtained at $\phi/\phi_0 = 0.5$ and the half-cycle repeats symmetrically up to the full AB period of $\phi = \phi_0$.

To verify the validity of our DLvN steady-state calculations, we compare the obtained results to the corresponding Landauer currents calculated within the nonequilibrium Green's function (NEGF) formalism with the MEHT Hamiltonian (see Appendix C for further details regarding the NEGF calculations). As can be seen, the NEGF results match well the DLvN calculations for both the 104° (red curve) and 180° (blue curve) connected systems with less than 5% maximal deviation at the peak regions.

As previously demonstrated, the behavior described above for the AB periods of the two model systems can be used to design molecular switching devices, where the external magnetic field threading the rings controls the current flowing through them.[23,30,40,55−59] These studies, however, focused on investigating the steady-state properties of such AB switches using Landauer's transport formalism combined with NEGF techniques to evaluate the transmittance probability of electrons through the system, as shown above. Notably, one of the most important properties of any switching device is its response time to the external control, which will dictate its operation frequency. The developed MEHT-DLvN methodology described herein allows the study of the intrinsic dynamical response of the system to the magnetic field control.

To demonstrate this, we performed electron dynamics simulations, where the system is initially prepared in a steady-state with no magnetic field, and analyze the transient dynamics of the system following an abrupt application of the magnetic field. This allows us to assess not only the response time required for the adjustment of the system to the new external conditions, but also the unique features appearing in the transient dynamics prior to settling into the new steady-state. In Figure 2a, we

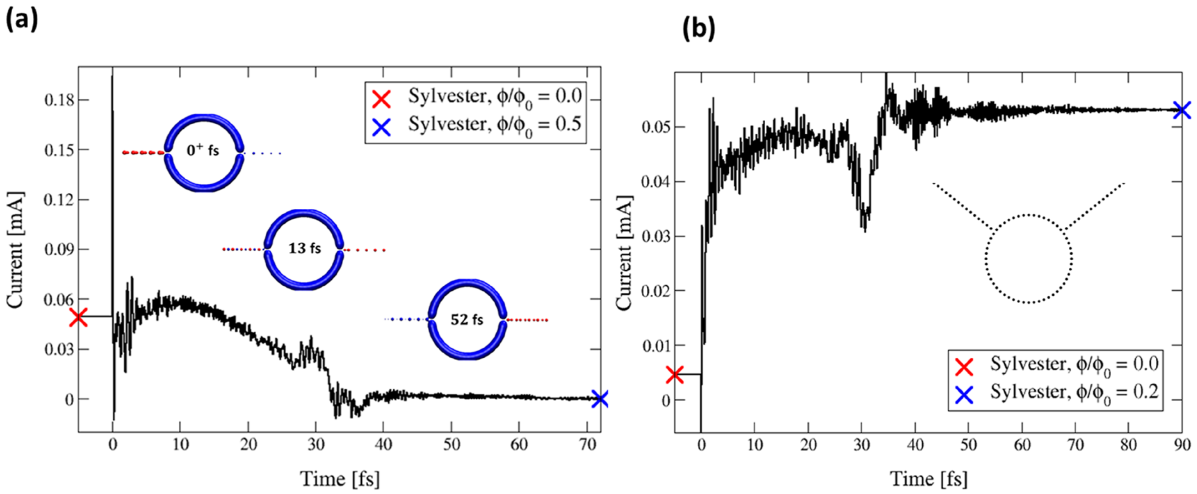

Figure 2. Current switching dynamics (obtained under a bias voltage of 1 V) in the (a) 180° and (b) 104° strongly coupled AB hydrogen rings due to the application of magnetic fluxes corresponding to $\phi = 0.5\phi_0$ and $\phi \approx 0.2\phi_0$, respectively. Snapshots of the variations in the electron density (with respect to the field-free steady-state density) during the transient dynamics region are shown in the insets of panel (a) at time frames of 0.01, 13, and 52 fs after switching on the magnetic-field. The isovalue used for the density differences plots is $\pm 4.72 \times 10^{-3}$ au. Steady-state current values obtained using the Sylvester equation in the absence and presence of the magnetic field are marked by the red and blue × marks, respectively.

present the current dynamics for the 180° strongly coupled system. As discussed above, with our specific choice of MEHT parameters[82] in the absence of a magnetic field, a steady-state on-current of 4.9×10^{-2} mA (red × mark) flows through the hydrogen ring. Upon the application of a magnetic flux of $\phi = 0.5\phi_0$ at time $t = 0$ fs strong current oscillations occur that can surpass the original steady-state current. These oscillations gradually decay toward the new steady-state ~50 fs after the application of the magnetic field, yielding an off-current of 2.0×10^{-5} mA (blue × mark). This exemplifies a ~50 fs switch-off time of the AB device with an on−off ratio of ~2460. We note here that the typical response time of the system (ring) to the application of the magnetic field is ~2.5 times that of the leads driving time toward their respective equilibrium states ($\Gamma^{-1} = 20$ fs) that is set by the density of lead states. In section 1 of the Supporting Information, we demonstrate that this ratio provides sufficiently converged dynamics.[76−78]

When plotting the electron density variations during the switch dynamics, we observe an immediate increase in the electron density on the ring. This persists throughout the dynamics until the new steady-state is achieved. At steady-state, we also observe electron density accumulation (depletion) at the lead section coupled to the source (drain). The fact that most of the density variations occur immediately after switching-on the field with minor variations throughout the rest of the dynamics toward the new steady-state indicates that the destructive interference responsible for the current suppression results only from the electron phase-shift between the two ring arms and is not reflected in the overall density variations.

The corresponding results for the 104° strongly coupled ring are presented in Figure 2b. Starting from a steady-state current of 4.7×10^{-3} mA (red × mark) in the absence of the magnetic field, when the field is switched on to provide a magnetic flux of $\phi \approx 0.2\phi_0$, strong current oscillations occur that are similar in nature to those observed for the 180° strongly coupled ring. Here, as well, the oscillations almost completely dampen after ~70 fs (see section 1 of the Supporting Information for a discussion on the relation between the system relaxation time-scales and the leads driving time-scales toward their respective equilibrium states) when the system reaches a new steady-state with an increased current of 5.3×10^{-2} mA (blue × mark). This demonstrates a 70 fs switch-on time of the AB device with an on−off ratio of ~11. The electron density variations on the ring upon field switch-on in this case are negligible compared to those obtained for the 180° connected ring. As mentioned above, this indicates that interference effects, rather than density variations, are responsible for the current increase.

In the context of Aharonov−Bohm molecular interferometers, the illustrative model systems introduced thus far require unrealistically high magnetic fields (of the order of hundreds of Tesla) to achieve substantial current switching. Higher device sensitivity can, however, be accomplished by increasing the cross-section of the molecular ring and/or by decreasing its coupling to the metallic leads.[23,30,40,55−59] To that end, we repeat the calculations presented above for the 52 atoms ring, now weakly coupled to two 2500 hydrogen atoms lead chains (see Supporting Information section 2 for convergence tests with respect to the lead model size) arranged at the 104° configuration (see the inset of Figure 3). To achieve weak ring-leads coupling we set the shortest distance between the ring and the lead atom closest to it to be 2.25 Å and leave all other interatomic distances at 1 Å. We note that contrary to the case of strongly coupled systems, where direct coupling of the ring to the driven lead sections should be avoided, in the weak-coupling limit the bare ring can be connected directly to the driven lead sections (without EM lead buffer regions). This allows us to eliminate unphysical features associated with the discrete nature of the extended molecule lead sections spectrum with minor effect on the calculated current profiles (see Supporting Information, section 4 for a detailed discussion of this issue).

Figure 3 shows the resulting steady-state currents flowing through the ring as a function of the normalized magnetic flux threading its cross section (black line). A sharp increase of the current from 2.0×10^{-5} to 1.2×10^{-3} mA followed by a plateau characterizes the low-field region of the AB period $\left(\frac{\phi}{\phi_0} < 0.25\right)$. Further increasing the magnetic flux threading the ring results in a significant current drop nearly to its field-free value at $\frac{\phi}{\phi_0} = 0.5$. The sharp increase at low fields can be attributed to the narrow

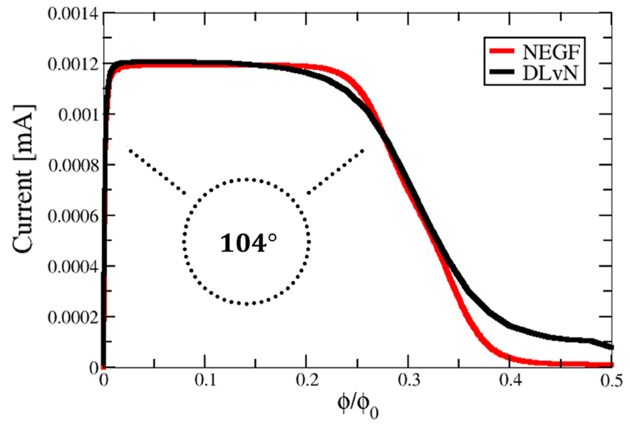

Figure 3. Steady-state current (obtained under a bias voltage of 1 V) vs the normalized magnetic flux threading an extended Hückel 52 hydrogen ring of diameter 1.66 nm that is weakly coupled to 2500 hydrogen atom chain leads arranged at angular separations of 104° calculated within the DLvN (black) and NEGF (red) models. Inset: the geometry of the molecular ring with the adjacent edges of the two lead models coupled to it. In the DLvN calculations a value of $\Gamma = 0.05\ \mathrm{fs}^{-1}$ was used.

resonances formed on the ring at the weak coupling limit that are shifted into the Fermi transport window by the magnetic-field.[55−57,59] Once inside the window, further increase of the magnetic field merely varies the resonance position within the window with little effect on the overall current until the level is shifted outside the Fermi window and the current drops. To further substantiate our DLvN results for the weakly coupled 104° connected ring, we repeated the steady-state calculations using NEGF (see red line in Figure 3). Overall, the agreement between the two calculations is quite good, with excellent correspondence at the low flux regime and somewhat narrower features in the NEGF calculation at the current drop region around $\phi/\phi_0 = 0.3$. Even better agreement can be obtained when increasing the size of the lead models in the DLvN calculations (see Supporting Information, section 1). Since in the present study we focus on the low-field switch-on region, we opt to use the 2500 hydrogen atom leads.

These results suggest that at the low coupling limit we should be able to switch the current of the weakly coupled 104° ring using a very low magnetic flux. To demonstrate the corresponding switching dynamics we prepared the system at steady-state in the absence of a magnetic field and followed the current dynamics after switching-on of a magnetic flux of $\phi = 0.005\phi_0$. As shown in Figure 4, in the absence of a magnetic field, a steady-state current of 1.7×10^{-5} mA (red × mark) flows through the hydrogen ring for an applied bias voltage of 1 V. Upon the application of the magnetic flux (time $t = 0$ fs) strong short-lasting (∼14 fs) current oscillations occur, followed by milder oscillations that slowly relax toward the new steady-state current of 1.1×10^{-3} mA (blue × mark) over a time-scale of ∼500 fs (see section 1 in the Supporting Information for a discussion on the relation between the system relaxation time-scales and the leads driving time scales toward their respective equilibrium states). The corresponding on−off ratio is ∼65. Notably, for the diameter of the considered hydrogen ring, the magnetic flux used herein corresponds to a switch-on magnetic field of 9.61 T for the weekly coupled system, which is considerably lower than the value of 384 T required to switch the current in the corresponding strongly coupled system.

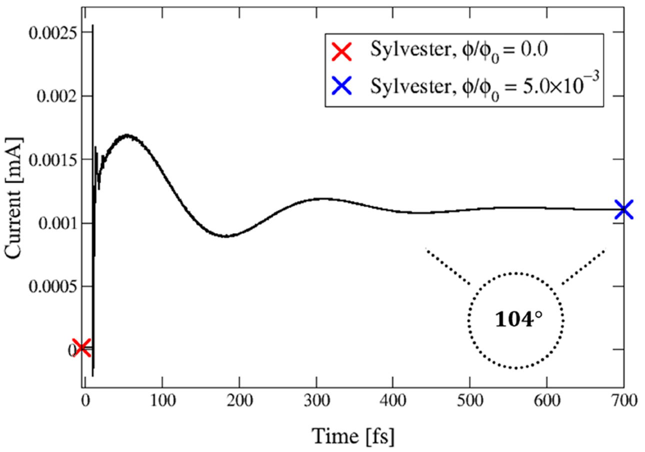

Figure 4. Current switching dynamics (obtained under a bias voltage of 1 V) in the 104° weakly coupled AB hydrogen rings due to the application of a magnetic flux corresponding to $\phi = 0.005\phi_0$. Steady-state current values obtained using the Sylvester equation in the absence and presence of the magnetic field are marked by the red and blue × marks, respectively.

■ SUMMARY AND CONCLUSIONS

The results presented above demonstrate the capabilities of the MEHT-DLvN methodology for simulating nonequilibrium electron dynamics in open quantum systems subjected to external varying magnetic fields. For strongly coupled molecular interferometers, unrealistically high magnetic fields are required to induce noticeable dynamics in the system. Increasing the sensitivity of the molecular device can be achieved by considering weakly coupled molecular rings. This allows us to develop molecular switches operating at feasible magnetic fields with dynamic time scales of the order of 500 fs. Since standard available technologies for magnetic field switching are typically slower than this value, our results indicate that the limiting factor of such a device would be the magnetic field control rather than the intrinsic response time of the system.[84] The developed method is not limited to the spinless extended Hückel electronic structure treatment used above and can be generalized to treat spin magnetic moment effects[90] and applied with any single-particle electronic structure treatment, such as time-dependent density functional theory.[85] Furthermore, the simplistic model systems considered herein were chosen to provide proof-of-concept demonstrations of the switching dynamics. Calculations on more realistic systems such as carbon nanotube junctions, which may exhibit different switching times and dynamics, the inclusion of a gate electrode, and implementations based on first-principles electronic structure treatments are currently being pursued.

■ APPENDIX A: DERIVATION OF THE SYLVESTER EQUATION FOR THE STEADY-STATE DENSITY MATRIX

The driven Liouville von Neumann equation of motion for a system consisting of an extended molecule section (EM), a left lead (L), and a right lead (R) that are not necessarily identical is given by the following block form:[66]

$$\frac{\mathrm{d}\hat{\boldsymbol{\rho}}}{\mathrm{d}t} = -\frac{i}{\hbar}[\tilde{\tilde{\boldsymbol{H}}}, \tilde{\tilde{\boldsymbol{\rho}}}] + \begin{pmatrix} -2\gamma_L\tilde{\tilde{\boldsymbol{\rho}}}_L + 2\gamma_L\tilde{\tilde{\boldsymbol{\rho}}}_L^0 & -\gamma_L\tilde{\tilde{\boldsymbol{\rho}}}_{L,EM} & -(\gamma_L+\gamma_R)\tilde{\tilde{\boldsymbol{\rho}}}_{L,R} \\ -\gamma_L\tilde{\tilde{\boldsymbol{\rho}}}_{EM,L} & \mathbf{0} & -\gamma_R\tilde{\tilde{\boldsymbol{\rho}}}_{EM,R} \\ -(\gamma_R+\gamma_L)\tilde{\tilde{\boldsymbol{\rho}}}_{R,L} & -\gamma_R\tilde{\tilde{\boldsymbol{\rho}}}_{R,EM} & -2\gamma_R\tilde{\tilde{\boldsymbol{\rho}}}_R + 2\gamma_R\tilde{\tilde{\boldsymbol{\rho}}}_R^0 \end{pmatrix} \tag{A1}$$

where $\tilde{\tilde{\boldsymbol{H}}}$ and $\tilde{\tilde{\boldsymbol{\rho}}}$ are the single particle Hamiltonian and density matrices of the entire system, respectively, given in the state representation,[66] $\tilde{\tilde{\boldsymbol{\rho}}}_{n,m}$ ($n,m = L, EM, R$) are the corresponding density matrix blocks, and γ_L and γ_R are the rates, at which the left and right leads are driven toward the equilibrium states of the baths to which they are implicitly coupled, respectively. By expanding the right-hand side of eq A1 we obtain the following equation:

$$\begin{aligned}\frac{\mathrm{d}\tilde{\tilde{\boldsymbol{\rho}}}}{\mathrm{d}t} &= -\frac{i}{\hbar}\tilde{\tilde{\boldsymbol{H}}}\tilde{\tilde{\boldsymbol{\rho}}} + \frac{i}{\hbar}\tilde{\tilde{\boldsymbol{\rho}}}\tilde{\tilde{\boldsymbol{H}}} - 2\gamma_L\begin{pmatrix}\tilde{\tilde{\boldsymbol{\rho}}}_L & \mathbf{0} & \mathbf{0}\\ \mathbf{0} & \mathbf{0} & \mathbf{0}\\ \mathbf{0} & \mathbf{0} & \mathbf{0}\end{pmatrix}\\ &- \gamma_L\begin{pmatrix}\mathbf{0} & \tilde{\tilde{\boldsymbol{\rho}}}_{L,EM} & \mathbf{0}\\ \mathbf{0} & \mathbf{0} & \mathbf{0}\\ \mathbf{0} & \mathbf{0} & \mathbf{0}\end{pmatrix} - (\gamma_L+\gamma_R)\begin{pmatrix}\mathbf{0} & \mathbf{0} & \tilde{\tilde{\boldsymbol{\rho}}}_{L,R}\\ \mathbf{0} & \mathbf{0} & \mathbf{0}\\ \mathbf{0} & \mathbf{0} & \mathbf{0}\end{pmatrix}\\ &- \gamma_L\begin{pmatrix}\mathbf{0} & \mathbf{0} & \mathbf{0}\\ \tilde{\tilde{\boldsymbol{\rho}}}_{EM,L} & \mathbf{0} & \mathbf{0}\\ \mathbf{0} & \mathbf{0} & \mathbf{0}\end{pmatrix} - \gamma_R\begin{pmatrix}\mathbf{0} & \mathbf{0} & \mathbf{0}\\ \mathbf{0} & \mathbf{0} & \tilde{\tilde{\boldsymbol{\rho}}}_{EM,R}\\ \mathbf{0} & \mathbf{0} & \mathbf{0}\end{pmatrix}\\ &- (\gamma_R+\gamma_L)\begin{pmatrix}\mathbf{0} & \mathbf{0} & \mathbf{0}\\ \mathbf{0} & \mathbf{0} & \mathbf{0}\\ \tilde{\tilde{\boldsymbol{\rho}}}_{R,L} & \mathbf{0} & \mathbf{0}\end{pmatrix} - \gamma_R\begin{pmatrix}\mathbf{0} & \mathbf{0} & \mathbf{0}\\ \mathbf{0} & \mathbf{0} & \mathbf{0}\\ \mathbf{0} & \tilde{\tilde{\boldsymbol{\rho}}}_{R,EM} & \mathbf{0}\end{pmatrix}\\ &- 2\gamma_R\begin{pmatrix}\mathbf{0} & \mathbf{0} & \mathbf{0}\\ \mathbf{0} & \mathbf{0} & \mathbf{0}\\ \mathbf{0} & \mathbf{0} & \tilde{\tilde{\boldsymbol{\rho}}}_R\end{pmatrix} + \begin{pmatrix}2\gamma_L\tilde{\tilde{\boldsymbol{\rho}}}_L^0 & \mathbf{0} & \mathbf{0}\\ \mathbf{0} & \mathbf{0} & \mathbf{0}\\ \mathbf{0} & \mathbf{0} & 2\gamma_R\tilde{\tilde{\boldsymbol{\rho}}}_R^0\end{pmatrix}\end{aligned} \tag{A2}$$

We may now define three projection matrices as follows:[75,79,81]

$$\boldsymbol{L} = \begin{pmatrix}\mathbf{1} & \mathbf{0} & \mathbf{0}\\ \mathbf{0} & \mathbf{0} & \mathbf{0}\\ \mathbf{0} & \mathbf{0} & \mathbf{0}\end{pmatrix}; \quad \boldsymbol{M} = \begin{pmatrix}\mathbf{0} & \mathbf{0} & \mathbf{0}\\ \mathbf{0} & \mathbf{1} & \mathbf{0}\\ \mathbf{0} & \mathbf{0} & \mathbf{0}\end{pmatrix}; \quad \boldsymbol{R} = \begin{pmatrix}\mathbf{0} & \mathbf{0} & \mathbf{0}\\ \mathbf{0} & \mathbf{0} & \mathbf{0}\\ \mathbf{0} & \mathbf{0} & \mathbf{1}\end{pmatrix} \tag{A3}$$

and rewrite eq A2 as

$$\begin{aligned}\frac{\mathrm{d}\tilde{\tilde{\boldsymbol{\rho}}}}{\mathrm{d}t} &= -\frac{i}{\hbar}\tilde{\tilde{\boldsymbol{H}}}\tilde{\tilde{\boldsymbol{\rho}}} + \frac{i}{\hbar}\tilde{\tilde{\boldsymbol{\rho}}}\tilde{\tilde{\boldsymbol{H}}} - 2\gamma_L\boldsymbol{L}\tilde{\tilde{\boldsymbol{\rho}}}\boldsymbol{L} - \gamma_L\boldsymbol{L}\tilde{\tilde{\boldsymbol{\rho}}}\boldsymbol{M} - \Gamma\boldsymbol{L}\tilde{\tilde{\boldsymbol{\rho}}}\boldsymbol{R}\\ &- \gamma_L\boldsymbol{M}\tilde{\tilde{\boldsymbol{\rho}}}\boldsymbol{L} - \gamma_R\boldsymbol{M}\tilde{\tilde{\boldsymbol{\rho}}}\boldsymbol{R} - \Gamma\boldsymbol{R}\tilde{\tilde{\boldsymbol{\rho}}}\boldsymbol{L} - \gamma_R\boldsymbol{R}\tilde{\tilde{\boldsymbol{\rho}}}\boldsymbol{M} - 2\gamma_R\boldsymbol{R}\tilde{\tilde{\boldsymbol{\rho}}}\boldsymbol{R}\\ &- \boldsymbol{C} = -\frac{i}{\hbar}\tilde{\tilde{\boldsymbol{H}}}\tilde{\tilde{\boldsymbol{\rho}}} - \gamma_L\boldsymbol{L}\tilde{\tilde{\boldsymbol{\rho}}}(\boldsymbol{L}+\boldsymbol{M}+\boldsymbol{R})\\ &- \gamma_R\boldsymbol{R}\tilde{\tilde{\boldsymbol{\rho}}}(\boldsymbol{L}+\boldsymbol{M}+\boldsymbol{R}) + \frac{i}{\hbar}\tilde{\tilde{\boldsymbol{\rho}}}\tilde{\tilde{\boldsymbol{H}}} - \gamma_L(\boldsymbol{L}+\boldsymbol{M}+\boldsymbol{R})\tilde{\tilde{\boldsymbol{\rho}}}\boldsymbol{L}\\ &- \gamma_R(\boldsymbol{L}+\boldsymbol{M}+\boldsymbol{R})\tilde{\tilde{\boldsymbol{\rho}}}\boldsymbol{R} - \boldsymbol{C}\end{aligned} \tag{A4}$$

where $\Gamma = \gamma_L + \gamma_R$ and $\boldsymbol{C} \equiv -\begin{pmatrix}2\gamma_L\tilde{\tilde{\boldsymbol{\rho}}}_L^0 & \mathbf{0} & \mathbf{0}\\ \mathbf{0} & \mathbf{0} & \mathbf{0}\\ \mathbf{0} & \mathbf{0} & 2\gamma_R\tilde{\tilde{\boldsymbol{\rho}}}_R^0\end{pmatrix}$. Using the relation $\boldsymbol{L} + \boldsymbol{M} + \boldsymbol{R} = \boldsymbol{I}$, $\boldsymbol{I}$ being the identity matrix of dimensions of the entire model system, eq A4 yields

$$\begin{aligned}\frac{\mathrm{d}\tilde{\tilde{\boldsymbol{\rho}}}}{\mathrm{d}t} &= \left(-\frac{i}{\hbar}\tilde{\tilde{\boldsymbol{H}}} - \gamma_L\boldsymbol{L} - \gamma_R\boldsymbol{R}\right)\tilde{\tilde{\boldsymbol{\rho}}} + \tilde{\tilde{\boldsymbol{\rho}}}\left(\frac{i}{\hbar}\tilde{\tilde{\boldsymbol{H}}} - \gamma_L\boldsymbol{L} - \gamma_R\boldsymbol{R}\right)\\ &- \boldsymbol{C}\end{aligned} \tag{A5}$$

When the left and right lead models are identical, their driving rates are taken to be identical, such that $\gamma_L = \gamma_R = \frac{\Gamma}{2}$ and eq A5 becomes

$$\begin{aligned}\frac{\mathrm{d}\tilde{\tilde{\boldsymbol{\rho}}}}{\mathrm{d}t} &= \left[-\frac{i}{\hbar}\tilde{\tilde{\boldsymbol{H}}} - \frac{\Gamma}{2}(\boldsymbol{L}+\boldsymbol{R})\right]\tilde{\tilde{\boldsymbol{\rho}}} + \tilde{\tilde{\boldsymbol{\rho}}}\left[\frac{i}{\hbar}\tilde{\tilde{\boldsymbol{H}}} - \frac{\Gamma}{2}(\boldsymbol{L}+\boldsymbol{R})\right]\\ &- \boldsymbol{C}\end{aligned} \tag{A6}$$

Defining

$$\boldsymbol{A} \equiv -\frac{i}{\hbar}\tilde{\tilde{\boldsymbol{H}}} - \frac{\Gamma}{2}(\boldsymbol{L}+\boldsymbol{R})$$

and $\boldsymbol{B} \equiv \frac{i}{\hbar}\tilde{\tilde{\boldsymbol{H}}} - \frac{\Gamma}{2}(\boldsymbol{L}+\boldsymbol{R})$, eq A6 can be rewritten as

$$\frac{\mathrm{d}\tilde{\tilde{\boldsymbol{\rho}}}}{\mathrm{d}t} = \boldsymbol{A}\tilde{\tilde{\boldsymbol{\rho}}} + \tilde{\tilde{\boldsymbol{\rho}}}\boldsymbol{B} - \boldsymbol{C} \tag{A7}$$

At steady-state the density matrix remains constant. Therefore, $\frac{\mathrm{d}\tilde{\tilde{\boldsymbol{\rho}}}}{\mathrm{d}t} = 0$ and we obtain

$$\boldsymbol{A}\tilde{\tilde{\boldsymbol{\rho}}}^{sts} + \tilde{\tilde{\boldsymbol{\rho}}}^{sts}\boldsymbol{B} = \boldsymbol{C} \tag{A8}$$

which is the Sylvester equation (eq 7 in the main text), whose solution gives the steady-state density matrix, $\tilde{\tilde{\boldsymbol{\rho}}}^{sts}$.

APPENDIX B. CURRENT EXPRESSION DERIVATION

To obtain an expression for the total current flowing through the system we start from eq 6 of the main text for the driven Liouville von Neumann equation of motion in the state-representation:[66]

$$\begin{aligned}\frac{\mathrm{d}\tilde{\tilde{\boldsymbol{\rho}}}}{\mathrm{d}t} &= -\frac{i}{\hbar}\left[\begin{pmatrix}\tilde{\tilde{\boldsymbol{H}}}_L & \tilde{\tilde{\boldsymbol{V}}}_{L,EM} & \mathbf{0}\\ \tilde{\tilde{\boldsymbol{V}}}_{EM,L} & \tilde{\tilde{\boldsymbol{H}}}_{EM} & \tilde{\tilde{\boldsymbol{V}}}_{EM,R}\\ \mathbf{0} & \tilde{\tilde{\boldsymbol{V}}}_{R,EM} & \tilde{\tilde{\boldsymbol{H}}}_R\end{pmatrix}, \begin{pmatrix}\tilde{\tilde{\boldsymbol{\rho}}}_L & \tilde{\tilde{\boldsymbol{\rho}}}_{L,EM} & \tilde{\tilde{\boldsymbol{\rho}}}_{L,R}\\ \tilde{\tilde{\boldsymbol{\rho}}}_{EM,L} & \tilde{\tilde{\boldsymbol{\rho}}}_{EM} & \tilde{\tilde{\boldsymbol{\rho}}}_{EM,R}\\ \tilde{\tilde{\boldsymbol{\rho}}}_{R.L} & \tilde{\tilde{\boldsymbol{\rho}}}_{R,EM} & \tilde{\tilde{\boldsymbol{\rho}}}_R\end{pmatrix}\right]\\ &- \Gamma\begin{pmatrix}\tilde{\tilde{\boldsymbol{\rho}}}_L - \tilde{\tilde{\boldsymbol{\rho}}}_L^0 & \frac{1}{2}\tilde{\tilde{\boldsymbol{\rho}}}_{L,EM} & \tilde{\tilde{\boldsymbol{\rho}}}_{L,R}\\ \frac{1}{2}\tilde{\tilde{\boldsymbol{\rho}}}_{EM,L} & \mathbf{0} & \frac{1}{2}\tilde{\tilde{\boldsymbol{\rho}}}_{EM,R}\\ \tilde{\tilde{\boldsymbol{\rho}}}_{R,L} & \frac{1}{2}\tilde{\tilde{\boldsymbol{\rho}}}_{R,EM} & \tilde{\tilde{\boldsymbol{\rho}}}_R - \tilde{\tilde{\boldsymbol{\rho}}}_R^0\end{pmatrix}\end{aligned} \tag{B1}$$

The propagation of the extended molecule block can be extracted from eq B1 to yield:

$$\begin{aligned}\frac{\mathrm{d}}{\mathrm{d}t}\tilde{\tilde{\boldsymbol{\rho}}}_{EM} &= -\frac{i}{\hbar}[(\tilde{\tilde{\mathbf{V}}}_{EM,L}\tilde{\tilde{\boldsymbol{\rho}}}_{L,EM} + \tilde{\tilde{\mathbf{H}}}_{EM}\tilde{\tilde{\boldsymbol{\rho}}}_{EM} + \tilde{\tilde{\mathbf{V}}}_{EM,R}\tilde{\tilde{\boldsymbol{\rho}}}_{R,EM}) \\ &\quad - (\tilde{\tilde{\boldsymbol{\rho}}}_{EM,L}\tilde{\tilde{\mathbf{V}}}_{L,EM} + \tilde{\tilde{\boldsymbol{\rho}}}_{EM}\tilde{\tilde{\mathbf{H}}}_{EM} + \tilde{\tilde{\boldsymbol{\rho}}}_{EM,R}\tilde{\tilde{\mathbf{V}}}_{R,EM})] \\ &= -\frac{i}{\hbar}[\tilde{\tilde{\mathbf{H}}}_{EM}, \tilde{\tilde{\boldsymbol{\rho}}}_{EM}] - \frac{i}{\hbar}(\tilde{\tilde{\mathbf{V}}}_{EM,L}\tilde{\tilde{\boldsymbol{\rho}}}_{L,EM} - \tilde{\tilde{\boldsymbol{\rho}}}_{EM,L}\tilde{\tilde{\mathbf{V}}}_{L,EM}) \\ &\quad - \frac{i}{\hbar}(\tilde{\tilde{\mathbf{V}}}_{EM,R}\tilde{\tilde{\boldsymbol{\rho}}}_{R,EM} - \tilde{\tilde{\boldsymbol{\rho}}}_{EM,R}\tilde{\tilde{\mathbf{V}}}_{R,EM})\end{aligned} \tag{B2}$$

The instantaneous number of electrons in the EM section is given by the trace of $\tilde{\tilde{\boldsymbol{\rho}}}_{EM}$, and its temporal variation is given by the corresponding time-derivative of the trace:

$$\begin{aligned}\dot{N}_{EM} &= \frac{\mathrm{d}}{\mathrm{d}t}\mathrm{Tr}(\tilde{\tilde{\boldsymbol{\rho}}}_{EM}) = \mathrm{Tr}\left(\frac{\mathrm{d}}{\mathrm{d}t}\tilde{\tilde{\boldsymbol{\rho}}}_{EM}\right) = -\frac{i}{\hbar}\underbrace{\mathrm{Tr}[\tilde{\tilde{\mathbf{H}}}_{EM}, \tilde{\tilde{\boldsymbol{\rho}}}_{EM}]}_{=0} \\ &\quad - \frac{i}{\hbar}\mathrm{Tr}(\tilde{\tilde{\mathbf{V}}}_{EM,L}\tilde{\tilde{\boldsymbol{\rho}}}_{L,EM} - \tilde{\tilde{\boldsymbol{\rho}}}_{EM,L}\tilde{\tilde{\mathbf{V}}}_{L,EM}) \\ &\quad - \frac{i}{\hbar}\mathrm{Tr}(\tilde{\tilde{\mathbf{V}}}_{EM,R}\tilde{\tilde{\boldsymbol{\rho}}}_{R,EM} - \tilde{\tilde{\boldsymbol{\rho}}}_{EM,R}\tilde{\tilde{\mathbf{V}}}_{R,EM})\end{aligned} \tag{B3}$$

The first term on the right-hand-side of eq B3 vanishes due to the cyclic property of the trace operator. The second and third terms can be simplified as follows:

$$\begin{aligned}&\mathrm{Tr}(\tilde{\tilde{\mathbf{V}}}_{EM,L/R}\tilde{\tilde{\boldsymbol{\rho}}}_{L/R,EM} - \tilde{\tilde{\boldsymbol{\rho}}}_{EM,L/R}\tilde{\tilde{\mathbf{V}}}_{L/R,EM}) \\ &\quad = \sum_{i}^{N_{EM}}\sum_{j}^{N_{L/R}}\{[\tilde{\tilde{\mathbf{V}}}_{EM,L/R}]_{i,j}[\tilde{\tilde{\boldsymbol{\rho}}}_{L/R,EM}]_{j,i} - [\tilde{\tilde{\boldsymbol{\rho}}}_{EM,L/R}]_{i,j} \\ &\quad [\tilde{\tilde{\mathbf{V}}}_{L/R,EM}]_{j,i}\} = \sum_{i}^{N_{EM}}\sum_{j}^{N_{L/R}}[[\tilde{\tilde{\mathbf{V}}}_{EM,L/R}]_{i,j}[\tilde{\tilde{\boldsymbol{\rho}}}_{L/R,EM}]_{j,i} \\ &\quad - [\tilde{\tilde{\boldsymbol{\rho}}}_{L/R,EM}]^{*}_{j,i}[\tilde{\tilde{\mathbf{V}}}_{EM,L/R}]^{*}_{i,j}]= \\ &\quad 2i\sum_{i}^{N_{EM}}\sum_{j}^{N_{L/R}}\mathrm{Im}\{[\tilde{\tilde{\mathbf{V}}}_{EM,L/R}]_{i,j}[\tilde{\tilde{\boldsymbol{\rho}}}_{L/R,EM}]_{j,i}\}\end{aligned} \tag{B4}$$

Here, the third transition is based on the Hermiticity of $\tilde{\tilde{\mathbf{V}}}_{n,m}$and $\tilde{\tilde{\boldsymbol{\rho}}}_{n,m}$, where their matrix elements satisfy the relations $[\tilde{\tilde{\mathbf{V}}}_{n,m}]_{i,j} = [\tilde{\tilde{\mathbf{V}}}_{m,n}]^{*}_{j,i}$ and $[\tilde{\tilde{\boldsymbol{\rho}}}_{n,m}]_{i,j} = [\tilde{\tilde{\boldsymbol{\rho}}}_{m,n}]^{*}_{j,i}$. Substituting eq B4 in eq B3 we obtain:

$$\begin{aligned}\dot{N}_{EM} &= \frac{2}{\hbar}\sum_{i}^{N_{EM}}\sum_{j}^{N_L}\mathrm{Im}\{[\tilde{\tilde{\mathbf{V}}}_{EM,L}]_{i,j}[\tilde{\tilde{\boldsymbol{\rho}}}_{L,EM}(t)]_{j,i}\} \\ &\quad + \frac{2}{\hbar}\sum_{i}^{N_{EM}}\sum_{j}^{N_R}\mathrm{Im}\{[\tilde{\tilde{\mathbf{V}}}_{EM,R}]_{i,j}[\tilde{\tilde{\boldsymbol{\rho}}}_{R,EM}(t)]_{j,i}\} \\ &= \frac{2}{\hbar}\sum_{i}^{N_{EM}}\sum_{j}^{N_L}\mathrm{Im}\{[\tilde{\tilde{\mathbf{V}}}_{EM,L}]_{i,j}[\tilde{\tilde{\boldsymbol{\rho}}}_{L,EM}(t)]_{j,i}\} \\ &\quad - \frac{2}{\hbar}\sum_{i}^{N_{EM}}\sum_{j}^{N_R}\mathrm{Im}\{[\tilde{\tilde{\mathbf{V}}}_{EM,R}]^{*}_{i,j}[\tilde{\tilde{\boldsymbol{\rho}}}_{R,EM}(t)]^{*}_{j,i}\} \\ &= \frac{2}{\hbar}\sum_{i}^{N_{EM}}\sum_{j}^{N_L}\mathrm{Im}\{[\tilde{\tilde{\mathbf{V}}}_{L,EM}]^{*}_{j,i}[\tilde{\tilde{\boldsymbol{\rho}}}_{L,EM}(t)]_{j,i}\} \\ &\quad - \frac{2}{\hbar}\sum_{i}^{N_{EM}}\sum_{j}^{N_R}\mathrm{Im}\{[\tilde{\tilde{\mathbf{V}}}_{EM,R}]^{*}_{i,j}[\tilde{\tilde{\boldsymbol{\rho}}}_{EM,R}(t)]_{i,j}\}\end{aligned} \tag{B5}$$

The term $J_L(t) \equiv \frac{2}{\hbar}\sum_{i}^{N_{EM}}\sum_{j}^{N_L}\mathrm{Im}\{[\tilde{\tilde{\mathbf{V}}}_{L,EM}]^{*}_{j,i}[\tilde{\tilde{\boldsymbol{\rho}}}_{L,EM}(t)]_{j,i}\}$ can be identified as the particle influx from the left lead into the extended molecule section, whereas the term

$$J_R(t) \equiv \frac{2}{\hbar}\sum_{i}^{N_{EM}}\sum_{j}^{N_R}\mathrm{Im}\{[\tilde{\tilde{\mathbf{V}}}_{EM,R}]^{*}_{i,j}[\tilde{\tilde{\boldsymbol{\rho}}}_{EM,R}(t)]_{i,j}\}$$

is the particles out-flux from the extended molecule section into the right lead. The total electronic current flowing through the system can be defined as the average of J_L and J_R times the electron charge. Adopting the standard definition of the current direction this gives eq 10 of the main text:

$$\begin{aligned}J(t) &= |e|\frac{[J_L(t) + J_R(t)]}{2} \\ &= \frac{|e|}{\hbar}\sum_{i}^{N_{EM}}\left[\sum_{j}^{N_L}\mathrm{Im}\{[\tilde{\tilde{\mathbf{V}}}_{L,EM}]^{*}_{j,i}[\tilde{\tilde{\boldsymbol{\rho}}}_{L,EM}(t)]_{j,i}\}\right. \\ &\quad \left. + \sum_{j}^{N_R}\mathrm{Im}\{[\tilde{\tilde{\mathbf{V}}}_{EM,R}]^{*}_{i,j}[\tilde{\tilde{\boldsymbol{\rho}}}_{EM,R}(t)]_{i,j}\}\right]\end{aligned} \tag{B6}$$

APPENDIX C: DESCRIPTION OF THE LANDAUER CURRENT CALCULATIONS USING THE NEGF FORMALISM

In order to validate the MEHT-DLvN model, the steady-state results calculated by solving eq 7 (derived in Appendix A) were benchmarked against the standard Landauer current evaluation[86] within the non-equilibrium Green function (NEGF) framework that has been previously used to calculate transport properties of Aharonov−Bohm molecular interferometers subjected to external magnetic fields.[57,59] The Landauer current is given by

$$J = \frac{2e}{h}\int N(E)[f(E;\, \mu_L,\, T_L) - f(E;\, \mu_R,\, T_R)]\, \mathrm{d}E \tag{C1}$$

where $f(E;\, \mu,\, T)$ is the Fermi−Dirac distribution given as a function of the leads' electronic temperature T, chemical potential μ, and energy E, and $N(E)$ is the transmittance probability of an electron to go through the system, which in the NEGF formalism has the following trace form:

$$N(\varepsilon) = \mathrm{Tr}[\mathbf{\Gamma}_L(\varepsilon)\mathbf{G}^{r}_{EM}(\varepsilon)\mathbf{\Gamma}_R(\varepsilon)\mathbf{G}^{a}_{EM}(\varepsilon)] \tag{C2}$$

Here, $\mathbf{G}^{r(a)}_{EM}(\varepsilon)$ is the retarded (advanced) Green function matrix representations of the device (extended molecule), and $\hat{\Gamma}_{L/R}(\varepsilon)$ are the broadening matrices due to the coupling of the device to the leads. To avoid numerical singularities in the calculation of the various GFs, we augment the real energy with a small imaginary part, $E \rightarrow \varepsilon \equiv E + i\eta$, such that the corresponding GF poles are shifted away from the real axis.

Both the device GF and the broadening matrices depend on the retarded (advanced) self-energy matrix $\mathbf{\Sigma}^{r(a)}_{L/R}(\varepsilon)$ in the following manner:

$$\mathbf{G}^{r}_{EM}(\varepsilon) = [\mathbf{G}^{a}_{EM}(\varepsilon)]^{\dagger} = [(\mathbf{G}^{r0}_{EM}(\varepsilon))^{-1} - \mathbf{\Sigma}^{r}_{L}(\varepsilon) - \mathbf{\Sigma}^{r}_{R}(\varepsilon)]^{-1} \tag{C3}$$

and:

$$\mathbf{\Gamma}_{L/R}(\varepsilon) = i[\mathbf{\Sigma}^{r}_{L/R}(\varepsilon) - \mathbf{\Sigma}^{a}_{L/R}(\varepsilon)] \tag{C4}$$

https://dx.doi.org/10.1021/acs.jpcc.0c01706
J. Phys. Chem. C 2020, 124, 8652−8662

where $\mathbf{G}^{r0}_{EM}(\varepsilon) = [\varepsilon \mathbf{S}_{EM} - \mathbf{H}_{EM}]^{-1}$ is the bare device's retarded GF given by its overlap $(\mathbf{S}_{EM})$ and Hamiltonian $(\mathbf{H}_{EM})$ matrices. The self-energy operators are given by

$$\begin{aligned}\mathbf{\Sigma}^{r}_{L/R}(\varepsilon) &= [\mathbf{\Sigma}^{a}_{L/R}(\varepsilon)]^{\dagger} \\ &= (\varepsilon \mathbf{S}_{EM,L/R} - \mathbf{V}_{EM,L/R})\mathbf{G}^{r0}_{L/R}(E) \\ &\quad (\varepsilon \mathbf{S}_{L/R,EM} - \mathbf{V}_{L/R,EM})\end{aligned} \tag{C5}$$

where $\mathbf{V}_{L/R,EM}$ and $\mathbf{S}_{L/R,EM}$ are the coupling and overlap matrices between the EM and the leads, respectively, and $\mathbf{G}^{r0}_{L/R}(\varepsilon) = [\varepsilon \mathbf{S}_{L/R} - \mathbf{H}_{L/R}]^{-1}$ is the bare leads' retarded GF. The evaluation of the latter invokes a computational challenge as the leads are treated as (semi)infinite. To that end, we adopt the iterative principal layer scheme originally developed by Sancho et al.[87−89] Here, a finite lead section, serving as a principle layer, is repeatedly duplicated in the direction pointing away from the device such as to extend the lead model until convergence of its electronic properties is achieved. Since each principle layer is identical to the rest, its appropriate intralayer $(\mathbf{H}^{00}_{L/R}, \mathbf{S}^{00}_{L/R})$ and interlayer $(\mathbf{V}^{01}_{L/R} = [\mathbf{V}^{10}_{L/R}]^{\dagger}, \mathbf{S}^{01}_{L/R} = [\mathbf{S}^{10}_{L/R}]^{\dagger})$ Hamiltonian and overlap matrices can be calculated only once, where one assumes that the next-nearest-principal-layer coupling and overlap can be neglected. With this the surface GF are given by

$$\mathbf{G}^{r0}_{L/R}(\varepsilon) = [(\varepsilon \mathbf{S}^{01}_{L/R} - \mathbf{V}^{01}_{L/R})\mathbf{T} + (\varepsilon \mathbf{S}^{00}_{L/R} - \mathbf{H}^{00}_{L/R})]^{-1} \tag{C6}$$

where $\mathbf{T}$ is the transfer matrix built iteratively in the following manner:

$$\mathbf{T} = \boldsymbol{t}_0 + \tilde{\boldsymbol{t}}_0\boldsymbol{t}_1 + \tilde{\boldsymbol{t}}_0\tilde{\boldsymbol{t}}_1\boldsymbol{t}_2 + \ldots + \tilde{\boldsymbol{t}}_0\tilde{\boldsymbol{t}}_1\tilde{\boldsymbol{t}}_2\ldots\tilde{\boldsymbol{t}}_{n-1}\boldsymbol{t}_n \tag{C7}$$

Here t_i, $\tilde{t}_i$ are a converging series defined recursively:

$$\boldsymbol{t}_i = \begin{cases}(\varepsilon \mathbf{S}^{00}_{L/R} - \mathbf{H}^{00}_{L/R})^{-1}(\mathbf{V}^{01}_{L/R})^{\dagger}, & i = 0 \\ (\mathbf{I}_{L/R} - \{\boldsymbol{t}_{i-1}, \tilde{\boldsymbol{t}}_{i-1}\})^{-1}\boldsymbol{t}^{2}{}_{i-1}, & i = 1, 2, \ldots, n\end{cases};$$

$$\tilde{\boldsymbol{t}}_i = \begin{cases}(\varepsilon \mathbf{S}^{00}_{L/R} - \mathbf{H}^{00}_{L/R})^{-1}\mathbf{V}^{01}_{L/R}, & i = 0 \\ (\mathbf{I}_{L/R} - \{\boldsymbol{t}_{i-1}, \tilde{\boldsymbol{t}}_{i-1}\})^{-1}\tilde{\boldsymbol{t}}^{2}{}_{i-1}, & i = 1, 2, \ldots, n\end{cases} \tag{C8}$$

where $\{A,B\} = AB + BA$ is the anticommutator of matrices $\mathbf{A}$ and $\mathbf{B}$ and $\mathbf{I}_{L/R}$ is a unit matrix of the corresponding lead dimension. n is determined by the expansion convergence criterion.

Upon convergence, the resulting transfer matrix can be plugged in eq C6, which gives the semi-infinite lead's surface GF. Next, the self-energies, broadening matrices, and device GF are computed according to eqs C5, C4, and C3, respectively, and the transmittance matrix is evaluated accordingly (eq C2). The various Hamiltonian matrix blocks used in these calculations are representations of the Hamiltonian operator given in eq 2 of the main text, such that the Landauer current computed via eq C1 depends on the value of the external magnetic field applied.

■ ASSOCIATED CONTENT

Supporting Information

The Supporting Information is available free of charge at https://pubs.acs.org/doi/10.1021/acs.jpcc.0c01706.

> Sensitivity test of the steady-state and dynamic currents with respect to the choice of driving rate, convergence test with respect to the finite lead model size, convergence test with respect to the width of the cutoff energy window, and an analysis of the effect of an extended molecule lead section in the case of weakly coupled rings (PDF)

■ AUTHOR INFORMATION

Corresponding Author

Oded Hod − *Department of Physical Chemistry, School of Chemistry, The Raymond and Beverly Sackler Faculty of Exact Sciences and The Sackler Center for Computational Molecular and Materials Science, Tel Aviv University, Tel Aviv 6997801, Israel;* orcid.org/0000-0003-3790-8613;
Email: odedhod@tauex.tau.ac.il

Author

Tal Maaravi − *Department of Physical Chemistry, School of Chemistry, The Raymond and Beverly Sackler Faculty of Exact Sciences and The Sackler Center for Computational Molecular and Materials Science, Tel Aviv University, Tel Aviv 6997801, Israel*

Complete contact information is available at:
https://pubs.acs.org/10.1021/acs.jpcc.0c01706

Notes

The authors declare no competing financial interest.

■ ACKNOWLEDGMENTS

We are grateful to Prof. Abraham Nitzan, Dr. Guy Cohen, and Dr. Michael Zwolak for helpful discussions, and to Prof. Yoram Selzer for his reference to relevant literature on experimental dynamic transport studies. O.H. is grateful for the generous financial support of the Israel Science Foundation under Grant No. 1740/13, The Ministry of Science and Technology of Israel under project number 3-16244, and the Center for Nanoscience and Nanotechnology of Tel-Aviv University.

■ REFERENCES

(1) Aviram, A.; Ratner, M. A. Molecular Rectifiers. *Chem. Phys. Lett.* **1974**, *29* (2), 277−283.

(2) Ghosh, A. *Nanoelectronics: A Molecular View*, 1st ed.; WSPC: Tokyo, 2016.

(3) Scheer, E.; Cuevas, J. C. *Molecular Electronics: An Introduction to Theory and Experiment*, 1st ed.; World Scientific Pub Co Inc.: Singapore and Hackensack, NJ, 2010.

(4) Nitzan, A.; Ratner, M. A. Electron Transport in Molecular Wire Junctions. *Science* **2003**, *300* (5624), 1384−1389.

(5) Editor. Does Molecular Electronics Compute? *Nat. Nanotechnol.* **2013**, *8* (6), 377.

(6) Ratner, M. A Brief History of Molecular Electronics. *Nat. Nanotechnol.* **2013**, *8*, 378−381.

(7) Editor. Visions for a Molecular Future. *Nat. Nanotechnol.* **2013**, *8*, 385−389.

(8) Blum, A. S.; Kushmerick, J. G.; Long, D. P.; Patterson, C. H.; Yang, J. C.; Henderson, J. C.; Yao, Y.; Tour, J. M.; Shashidhar, R.; Ratna, B. R. Molecularly Inherent Voltage-Controlled Conductance Switching. *Nat. Mater.* **2005**, *4* (2), 167−172.

(9) Stuyver, T.; Fias, S.; Geerlings, P.; De Proft, F.; Alonso, M. Qualitative Insights into the Transport Properties of Hückel/Möbius (Anti)Aromatic Compounds: Application to Expanded Porphyrins. *J. Phys. Chem. C* **2018**, *122* (34), 19842−19856.

(10) Dell, E. J.; Capozzi, B.; Xia, J.; Venkataraman, L.; Campos, L. M. Molecular Length Dictates the Nature of Charge Carriers in Single-Molecule Junctions of Oxidized Oligothiophenes. *Nat. Chem.* **2015**, *7* (3), 209−214.

(11) Díez-Pérez, I.; Hihath, J.; Lee, Y.; Yu, L.; Adamska, L.; Kozhushner, M. A.; Oleynik, I. I.; Tao, N. Rectification and Stability

of a Single Molecular Diode with Controlled Orientation. *Nat. Chem.* **2009**, *1* (8), 635−641.

(12) Solomon, G. C.; Herrmann, C.; Hansen, T.; Mujica, V.; Ratner, M. A. Exploring Local Currents in Molecular Junctions. *Nat. Chem.* **2010**, *2* (3), 223−228.

(13) Miller, J. R. Electron Transfer: Lower Tunnel Barriers. *Nat. Chem.* **2014**, *6* (10), 854−855.

(14) Hu, L.; Guo, Y.; Yan, X.; Zeng, H.; Zhou, J. Electronic Transport Properties in [n]Cycloparaphenylenes Molecular Devices. *Phys. Lett. A* **2017**, *381* (25), 2107−2111.

(15) Rakhmilevitch, D.; Sarkar, S.; Bitton, O.; Kronik, L.; Tal, O. Enhanced Magnetoresistance in Molecular Junctions by Geometrical Optimization of Spin-Selective Orbital Hybridization. *Nano Lett.* **2016**, *16* (3), 1741−1745.

(16) Jia, C.; Guo, X. Molecule−Electrode Interfaces in Molecular Electronic Devices. *Chem. Soc. Rev.* **2013**, *42* (13), 5642−5660.

(17) Zelovich, T.; Kronik, L.; Hod, O. Molecule−Lead Coupling at Molecular Junctions: Relation between the Real- and State-Space Perspectives. *J. Chem. Theory Comput.* **2015**, *11* (10), 4861−4869.

(18) Yaliraki, S. N.; Ratner, M. A. Molecule-Interface Coupling Effects on Electronic Transport in Molecular Wires. *J. Chem. Phys.* **1998**, *109* (12), 5036−5043.

(19) Champagne, A. R.; Pasupathy, A. N.; Ralph, D. C. Mechanically Adjustable and Electrically Gated Single-Molecule Transistors. *Nano Lett.* **2005**, *5* (2), 305−308.

(20) Martínez-Blanco, J.; Nacci, C.; Erwin, S. C.; Kanisawa, K.; Locane, E.; Thomas, M.; von Oppen, F.; Brouwer, P. W.; Fölsch, S. Gating a Single-Molecule Transistor with Individual Atoms. *Nat. Phys.* **2015**, *11* (8), 640−644.

(21) Zhitenev, N. B.; Meng, H.; Bao, Z. Conductance of Small Molecular Junctions. *Phys. Rev. Lett.* **2002**, *88* (22), 226801.

(22) van der Zant, H. S. J.; Kervennic, Y.-V.; Poot, M.; O'Neill, K.; de Groot, Z.; Thijssen, J. M.; Heersche, H. B.; Stuhr-Hansen, N.; Bjørnholm, T.; Vanmaekelbergh, D.; et al. Molecular Three-Terminal Devices: Fabrication and Measurements. *Faraday Discuss.* **2006**, *131* (0), 347−356.

(23) Rai, D.; Hod, O.; Nitzan, A. Magnetic Field Control of the Current through Molecular Ring Junctions. *J. Phys. Chem. Lett.* **2011**, *2* (17), 2118−2124.

(24) Yadalam, H. K.; Harbola, U. Controlling Local Currents in Molecular Junctions. *Phys. Rev. B: Condens. Matter Mater. Phys.* **2016**, *94* (11), 115424.

(25) Petreska, I.; Pejov, L.; Kocarev, L. Exploring the Possibilities to Control the Molecular Switching Properties and Dynamics: A Field-Switchable Rotor-Stator Molecular System. *J. Chem. Phys.* **2011**, *134* (1), 014708.

(26) Donhauser, Z. J.; Mantooth, B. A.; Kelly, K. F.; Bumm, L. A.; Monnell, J. D.; Stapleton, J. J.; Price, D. W.; Rawlett, A. M.; Allara, D. L.; Tour, J. M.; et al. Conductance Switching in Single Molecules Through Conformational Changes. *Science* **2001**, *292* (5525), 2303−2307.

(27) Quek, S. Y.; Kamenetska, M.; Steigerwald, M. L.; Choi, H. J.; Louie, S. G.; Hybertsen, M. S.; Neaton, J. B.; Venkataraman, L. Mechanically Controlled Binary Conductance Switching of a Single-Molecule Junction. *Nat. Nanotechnol.* **2009**, *4* (4), 230−234.

(28) Sotthewes, K.; Geskin, V.; Heimbuch, R.; Kumar, A.; Zandvliet, H. J. W. Research Update: Molecular Electronics: The Single-Molecule Switch and Transistor. *APL Mater.* **2014**, *2* (1), 010701.

(29) Li, Z.; Li, H.; Chen, S.; Froehlich, T.; Yi, C.; Schönenberger, C.; Calame, M.; Decurtins, S.; Liu, S.-X.; Borguet, E. Regulating a Benzodifuran Single Molecule Redox Switch via Electrochemical Gating and Optimization of Molecule/Electrode Coupling. *J. Am. Chem. Soc.* **2014**, *136* (25), 8867−8870.

(30) Hod, O.; Baer, R.; Rabani, E. A Parallel Electromagnetic Molecular Logic Gate. *J. Am. Chem. Soc.* **2005**, *127* (6), 1648−1649.

(31) Stokbro, K.; Taylor, J.; Brandbyge, M. Do Aviram−Ratner Diodes Rectify? *J. Am. Chem. Soc.* **2003**, *125* (13), 3674−3675.

(32) Capozzi, B.; Xia, J.; Adak, O.; Dell, E. J.; Liu, Z.-F.; Taylor, J. C.; Neaton, J. B.; Campos, L. M.; Venkataraman, L. Single-Molecule Diodes with High Rectification Ratios through Environmental Control. *Nat. Nanotechnol.* **2015**, *10* (6), 522−527.

(33) Zhang, G.; Ratner, M. A.; Reuter, M. G. Is Molecular Rectification Caused by Asymmetric Electrode Couplings or by a Molecular Bias Drop? *J. Phys. Chem. C* **2015**, *119* (11), 6254−6260.

(34) Yuan, L.; Nerngchamnong, N.; Cao, L.; Hamoudi, H.; del Barco, E.; Roemer, M.; Sriramula, R. K.; Thompson, D.; Nijhuis, C. A. Controlling the Direction of Rectification in a Molecular Diode. *Nat. Commun.* **2015**, *6*, 6324.

(35) Segal, D.; Nitzan, A. Molecular Heat Pump. *Phys. Rev. E* **2006**, *73* (2), 026109.

(36) Segal, D. Vibrational Relaxation in the Kubo Oscillator: Stochastic Pumping of Heat. *J. Chem. Phys.* **2009**, *130* (13), 134510.

(37) Nitzan, A. Molecules Take the Heat. *Science* **2007**, *317* (5839), 759−760.

(38) Schmaus, S.; Bagrets, A.; Nahas, Y.; Yamada, T. K.; Bork, A.; Bowen, M.; Beaurepaire, E.; Evers, F.; Wulfhekel, W. Giant Magnetoresistance through a Single Molecule. *Nat. Nanotechnol.* **2011**, *6* (3), 185−189.

(39) Rai, D.; Hod, O.; Nitzan, A. Circular Currents in Molecular Wires. *J. Phys. Chem. C* **2010**, *114* (48), 20583−20594.

(40) Rai, D.; Hod, O.; Nitzan, A. Magnetic Fields Effects on the Electronic Conduction Properties of Molecular Ring Structures. *Phys. Rev. B: Condens. Matter Mater. Phys.* **2012**, *85* (15), 155440.

(41) Borges, A.; Fung, E.-D.; Ng, F.; Venkataraman, L.; Solomon, G. C. Probing the Conductance of the σ-System of Bipyridine Using Destructive Interference. *J. Phys. Chem. Lett.* **2016**, *7* (23), 4825−4829.

(42) Borges, A.; Xia, J.; Liu, S. H.; Venkataraman, L.; Solomon, G. C. The Role of Through-Space Interactions in Modulating Constructive and Destructive Interference Effects in Benzene. *Nano Lett.* **2017**, *17* (7), 4436−4442.

(43) Garner, M. H.; Li, H.; Chen, Y.; Su, T. A.; Shangguan, Z.; Paley, D. W.; Liu, T.; Ng, F.; Li, H.; Xiao, S.; et al. Comprehensive Suppression of Single-Molecule Conductance Using Destructive σ-Interference. *Nature* **2018**, *558* (7710), 415−419.

(44) Walz, M.; Wilhelm, J.; Evers, F. Current Patterns and Orbital Magnetism in Mesoscopic Dc Transport. *Phys. Rev. Lett.* **2014**, *113* (13), 136602.

(45) Patra, M.; Maiti, S. K. Modulation of Circular Current and Associated Magnetic Field in a Molecular Junction: A New Approach. *Sci. Rep.* **2017**, *7*, 43343.

(46) Guédon, C. M.; Valkenier, H.; Markussen, T.; Thygesen, K. S.; Hummelen, J. C.; van der Molen, S. J. Observation of Quantum Interference in Molecular Charge Transport. *Nat. Nanotechnol.* **2012**, *7* (5), 305−309.

(47) Vazquez, H.; Skouta, R.; Schneebeli, S.; Kamenetska, M.; Breslow, R.; Venkataraman, L.; Hybertsen, M. S. Probing the Conductance Superposition Law in Single-Molecule Circuits with Parallel Paths. *Nat. Nanotechnol.* **2012**, *7* (10), 663−667.

(48) Li, Y.; Buerkle, M.; Li, G.; Rostamian, A.; Wang, H.; Wang, Z.; Bowler, D. R.; Miyazaki, T.; Xiang, L.; Asai, Y.; et al. Gate Controlling of Quantum Interference and Direct Observation of Anti-Resonances in Single Molecule Charge Transport. *Nat. Mater.* **2019**, *18* (4), 357−363.

(49) Sam-ang, P.; Reuter, M. G. Characterizing Destructive Quantum Interference in Electron Transport. *New J. Phys.* **2017**, *19* (5), 053002.

(50) Aharonov, Y.; Bohm, D. Significance of Electromagnetic Potentials in the Quantum Theory. *Phys. Rev.* **1959**, *115* (3), 485−491.

(51) Aharonov, Y.; Bohm, D. Further Considerations on Electromagnetic Potentials in the Quantum Theory. *Phys. Rev.* **1961**, *123* (4), 1511−1524.

(52) Roche, S.; Triozon, F.; Rubio, A. Backscattering in Carbon Nanotubes: Role of Quantum Interference Effects. *Appl. Phys. Lett.* **2001**, *79* (22), 3690−3692.

(53) Coskun, U. C.; Wei, T.-C.; Vishveshwara, S.; Goldbart, P. M.; Bezryadin, A. H/e Magnetic Flux Modulation of the Energy Gap in Nanotube Quantum Dots. *Science* **2004**, *304* (5674), 1132−1134.

(54) Zaric, S.; Ostojic, G. N.; Kono, J.; Shaver, J.; Moore, V. C.; Strano, M. S.; Hauge, R. H.; Smalley, R. E.; Wei, X. Optical Signatures

of the Aharonov-Bohm Phase in Single-Walled Carbon Nanotubes. *Science* **2004**, *304* (5674), 1129−1131.

(55) Hod, O.; Rabani, E.; Baer, R. Magnetoresistance Devices Based on Single-Walled Carbon Nanotubes. *J. Chem. Phys.* **2005**, *123* (5), 051103.

(56) Hod, O.; Baer, R.; Rabani, E. Feasible Nanometric Magnetoresistance Devices. *J. Phys. Chem. B* **2004**, *108* (39), 14807−14810.

(57) Hod, O.; Rabani, E.; Baer, R. Magnetoresistance of Nanoscale Molecular Devices. *Acc. Chem. Res.* **2006**, *39* (2), 109−117.

(58) Hod, O.; Baer, R.; Rabani, E. Inelastic Effects in Aharonov-Bohm Molecular Interferometers. *Phys. Rev. Lett.* **2006**, *97* (26), 266803.

(59) Hod, O.; Baer, R.; Rabani, E. Magnetoresistance of Nanoscale Molecular Devices Based on Aharonov−Bohm Interferometry. *J. Phys.: Condens. Matter* **2008**, *20* (38), 383201.

(60) Selzer, Y.; Peskin, U. Transient Dynamics in Molecular Junctions: Picosecond Resolution from Dc Measurements by a Laser Pulse Pair Sequence Excitation. *J. Phys. Chem. C* **2013**, *117* (43), 22369−22376.

(61) Lumbroso, O. S.; Simine, L.; Nitzan, A.; Segal, D.; Tal, O. Electronic Noise Due to Temperature Differences in Atomic-Scale Junctions. *Nature* **2018**, *562* (7726), 240.

(62) Li, Y.; Zolotavin, P.; Doak, P.; Kronik, L.; Neaton, J. B.; Natelson, D. Interplay of Bias-Driven Charging and the Vibrational Stark Effect in Molecular Junctions. *Nano Lett.* **2016**, *16* (2), 1104−1109.

(63) Batra, A.; Kladnik, G.; Vázquez, H.; Meisner, J. S.; Floreano, L.; Nuckolls, C.; Cvetko, D.; Morgante, A.; Venkataraman, L. Quantifying Through-Space Charge Transfer Dynamics in π-Coupled Molecular Systems. *Nat. Commun.* **2012**, *3*, 1086.

(64) Ravikumar, A.; Kladnik, G.; Müller, M.; Cossaro, A.; Bavdek, G.; Patera, L. L.; Sánchez-Portal, D.; Venkataraman, L.; Morgante, A.; Brivio, G. P.; et al. Tuning Ultrafast Electron Injection Dynamics at Organic-Graphene/Metal Interfaces. *Nanoscale* **2018**, *10* (17), 8014−8022.

(65) Bruch, A.; Thomas, M.; Viola Kusminskiy, S.; von Oppen, F.; Nitzan, A. Quantum Thermodynamics of the Driven Resonant Level Model. *Phys. Rev. B: Condens. Matter Mater. Phys.* **2016**, *93* (11), 115318.

(66) Zelovich, T.; Kronik, L.; Hod, O. State Representation Approach for Atomistic Time-Dependent Transport Calculations in Molecular Junctions. *J. Chem. Theory Comput.* **2014**, *10* (8), 2927−2941.

(67) Hod, O.; Rodríguez-Rosario, C. A.; Zelovich, T.; Frauenheim, T. Driven Liouville von Neumann Equation in Lindblad Form. *J. Phys. Chem. A* **2016**, *120* (19), 3278−3285.

(68) Zelovich, T.; Kronik, L.; Hod, O. Driven Liouville von Neumann Approach for Time-Dependent Electronic Transport Calculations in a Nonorthogonal Basis-Set Representation. *J. Phys. Chem. C* **2016**, *120* (28), 15052−15062.

(69) Zelovich, T.; Hansen, T.; Liu, Z.-F.; Neaton, J. B.; Kronik, L.; Hod, O. Parameter-Free Driven Liouville-von Neumann Approach for Time-Dependent Electronic Transport Simulations in Open Quantum Systems. *J. Chem. Phys.* **2017**, *146* (9), 092331.

(70) Toroker, M. C.; Peskin, U. On the Relation between Steady-State Currents and Resonance States in Molecular Junctions. *J. Phys. B: At., Mol. Opt. Phys.* **2009**, *42* (4), 044013.

(71) London, F. Théorie quantique des courants interatomiques dans les combinaisons aromatiques. *J. Phys. Radium* **1937**, *8* (10), 397−409.

(72) Pople, J. A. Molecular-Orbital Theory of Diamagnetism. I. An Approximate LCAO Scheme. *J. Chem. Phys.* **1962**, *37* (1), 53−59.

(73) Kwok, Y. H.; Xie, H.; Yam, C. Y.; Zheng, X.; Chen, G. H. Time-Dependent Density Functional Theory Quantum Transport Simulation in Non-Orthogonal Basis. *J. Chem. Phys.* **2013**, *139* (22), 224111.

(74) Zelovich, T.; Kronik, L.; Hod, O. Driven Liouville von Neumann Approach for Time-Dependent Electronic Transport Calculations in a Nonorthogonal Basis-Set Representation. *J. Phys. Chem. C* **2016**, *120* (28), 15052−15062.

(75) Subotnik, J. E.; Hansen, T.; Ratner, M. A.; Nitzan, A. Nonequilibrium Steady State Transport via the Reduced Density Matrix Operator. *J. Chem. Phys.* **2009**, *130* (14), 144105.

(76) Elenewski, J. E.; Gruss, D.; Zwolak, M. Communication: Master Equations for Electron Transport: The Limits of the Markovian Limit. *J. Chem. Phys.* **2017**, *147* (15), 151101.

(77) Gruss, D.; Smolyanitsky, A.; Zwolak, M. Communication: Relaxation-Limited Electronic Currents in Extended Reservoir Simulations. *J. Chem. Phys.* **2017**, *147* (14), 141102.

(78) Gruss, D.; Velizhanin, K. A.; Zwolak, M. Landauer's Formula with Finite-Time Relaxation: Kramers' Crossover in Electronic Transport. *Sci. Rep.* **2016**, *6*, 24514.

(79) Oz, I.; Hod, O.; Nitzan, A. Evaluation of Dynamical Properties of Open Quantum Systems Using the Driven Liouville-von Neumann Approach: Methodological Considerations. *Mol. Phys.* **2019**, *117* (15−16), 2083−2096.

(80) Ramírez, F.; Dundas, D.; Sánchez, C. G.; Scherlis, D. A.; Todorov, T. N. Driven Liouville−von Neumann Equation for Quantum Transport and Multiple-Probe Green's Functions. *J. Phys. Chem. C* **2019**, *123* (20), 12542−12555.

(81) Oz, A.; Hod, O.; Nitzan, A. A Numerical Approach to Non-Equilibrium Quantum Thermodynamics: Non-Perturbative Treatment of the Driven Resonant Level Model Based on the Driven Liouville von-Neumann Formalism. *J. Chem. Theory Comput.* **2020**, *16*, 1232.

(82) Hoffmann, R. An Extended Hückel Theory. I. Hydrocarbons. *J. Chem. Phys.* **1963**, *39* (6), 1397−1412.

(83) Press, W. H.; Teukolsky, S. A.; Vetterling, W. T.; Flannery, B. P. Numerical Recipes. *The Art of Scientific Computing*, 3rd ed.; Cambridge University Press: Cambridge, U.K., and New York, 2007.

(84) Barman, A.; Haldar, A. Time-Domain Study of Magnetization Dynamics in Magnetic Thin Films and Micro- and Nanostructures. *Solid State Phys.* **2014**, *65*, 1−108.

(85) Morzan, U. N.; Ramírez, F. F.; González Lebrero, M. C.; Scherlis, D. A. Electron Transport in Real Time from First-Principles. *J. Chem. Phys.* **2017**, *146* (4), 044110.

(86) Landauer, R. Spatial Variation of Currents and Fields Due to Localized Scatterers in Metallic Conduction. *IBM J. Res. Dev.* **1957**, *1* (3), 223−231.

(87) Sancho, M. P. L.; Sancho, J. M. L.; Rubio, J. Quick Iterative Scheme for the Calculation of Transfer Matrices: Application to Mo (100). *J. Phys. F: Met. Phys.* **1984**, *14* (5), 1205−1215.

(88) Sancho, M. P.; Sancho, J. M. L.; Sancho, J. M. L.; Rubio, J. Highly Convergent Schemes for the Calculation of Bulk and Surface Green Functions. *J. Phys. F: Met. Phys.* **1985**, *15*, 851.

(89) Sancho, M. P. L.; Sancho, J. M. L.; Rubio, J. A Nonorthogonal-Basis Calculation of the Spectral Density of Surface States for the (100) and (110) Faces of Tungsten. *J. Phys. C: Solid State Phys.* **1985**, *18* (9), 1803−1815.

(90) Cohen, G.; Hod, O.; Rabani, E. Constructing Spin Interference Devices from Nanometric Rings. *Phys. Rev. B: Condens. Matter Mater. Phys.* **2007**, *76*, No. 235120.